atmosphere

MDPI

Article

Spatiotemporal Ionospheric TEC Prediction with Deformable Convolution for Long-Term Spatial Dependencies

Jie Li [1], Jian Xiao [2,*], Haijun Liu [2], Xiaofeng Du [1] and Shixiang Liu [1]

[1] China National Offshore Oil Corporation Research Institute, Co., Ltd., Beijing 100028, China; lijie78@cnooc.com.cn (J.L.); duxf@cnooc.com.cn (X.D.); liushx2@cnooc.com.cn (S.L.)
[2] Institute of Intelligent Emergency Information Processing, Institute of Disaster Prevention, Langfang 065201, China; liuhaijun@cidp.edu.cn
* Correspondence: 23661630@st.cidp.edu.cn

Abstract

SA-ConvLSTM is a recently proposed spatiotemporal model for total electron content (TEC) prediction, which effectively catches long-term temporal evolution and global-scale spatial correlations in TEC. However, its reliance on standard convolution limits spatial feature extraction to fixed regular regions, reducing the flexibility for irregular TEC variations. To address this limitation, we enhance SA-ConvLSTM by incorporating deformable convolution, proposing SA-DConvLSTM. This achieves adaptive spatial feature extraction through learnable offsets in convolutional kernels. Building on this improvement, we design ED-SA-DConvLSTM, a TEC spatiotemporal prediction model based on an encoder–decoder architecture with SA-DConvLSTM as its fundamental block. Firstly, the effectiveness of the model improvement was verified through an ablation experiment. Subsequently, a comprehensive quantitative comparison was conducted between ED-SA-DConvLSTM and baseline models (C1PG, ConvLSTM, and ConvGRU) in the region of 12.5° S–87.5° N and 25° E–180° E. The experimental results showed that the ED-SA-DConvLSTM exhibited superior performance compared to C1PG, ConvGRU, and ConvLSTM, with prediction accuracy improvements of 10.27%, 7.65%, and 7.16% during high solar activity and 11.46%, 4.75%, and 4.06% during low solar activity, respectively. To further evaluate model performance under extreme conditions, we tested the ED-SA-DConvLSTM during four geomagnetic storms. The results showed that the proportion of its superiority over the baseline models exceeded 58%.

Keywords: total electron content; long-term spatial dependencies; spatiotemporal prediction; deformable convolution

check for updates

Academic Editor: Stelios M. Potirakis

Received: 10 July 2025
Revised: 1 August 2025
Accepted: 6 August 2025
Published: 7 August 2025

Citation: Li, J.; Xiao, J.; Liu, H.; Du, X.; Liu, S. Spatiotemporal Ionospheric TEC Prediction with Deformable Convolution for Long-Term Spatial Dependencies. *Atmosphere* **2025**, *16*, 950. https://doi.org/10.3390/atmos16080950

Copyright: © 2025 by the authors. Licensee MDPI, Basel, Switzerland. This article is an open access article distributed under the terms and conditions of the Creative Commons Attribution (CC BY) license (https://creativecommons.org/licenses/by/4.0/).

1. Introduction

The ionosphere, an ionized region of Earth's upper atmosphere, contains abundant charged particles that influence electromagnetic wave propagation through velocity and path alterations, causing ionospheric delay [1]. Ionospheric delay is the primary error source in Global Navigation Satellite System (GNSS) applications [2,3]. The ionosphere total electron content (TEC) is an important parameter for describing the ionosphere [4], which can be used to calculate ionospheric delay [5,6]. Accurate TEC prediction enables precise ionospheric delay correction, thereby enhancing the reliability and accuracy of GNSS-based positioning, navigation, and timing services [7,8].

The TEC exhibits complex spatiotemporal variations driven by multiple geophysical factors including local time, seasonal cycles, solar activity levels, and geomagnetic condi-

tions. These complex changes pose a great challenge to accurately predicting TEC [9–11]. Deep learning methods have emerged as powerful tools for this task due to their superior capacity in modeling nonlinear relationships [12–14], demonstrating remarkable success across various prediction applications [15–17].

There are currently two main deep learning methods used for TEC prediction: (1) Time series models, which consider TEC prediction as time series prediction. Early implementations adopted basic recurrent architectures such as LSTM [18–20] and GRU [21], which were subsequently enhanced through bidirectional variants offering improved temporal modeling capabilities [22,23]. The field then progressed to hybrid architectures combining convolutional layers with recurrent networks to capture both temporal patterns and local spatial features [24–26]. Most recently, attention mechanisms have been successfully integrated into these frameworks to enable dynamic feature weighting [27,28]. While these temporal approaches have achieved reasonable performance, they are fundamentally limited by their inability to incorporate broader spatial correlations. (2) Spatiotemporal models. This kind of model processes the continuous TEC map sequences by convolution operation and realizes the dual feature extraction of the temporal and spatial features of TEC. Therefore, its prediction effect is often superior to those of time series models. Among them, the most famous spatiotemporal prediction model is ConvLSTM [29]. In recent years, it and its variants have been widely used in TEC prediction [30,31], including Attention ConvLSTM [32], ED-ConvLSTM [33–35], ConvGRU [36], BiConvGRU [37], etc.

While spatiotemporal models such as ConvLSTM and ConvGRU currently dominate TEC prediction, they face two critical limitations. One of the challenges faced by TEC prediction is how to effectively model the long-term spatial correlation of TEC. Although the existing spatial–temporal model based on ConvLSTM can effectively capture local spatial features, in order to capture long-term spatial features, it is necessary to stack multiple convolution layers. However, the inherent limitations of convolution operation will cause the effective receptive field to be much smaller than the theoretical receptive field, which makes the long-term correlation modeling inefficient [38]. Another issue is the shape of the convolution kernel. Most existing models use standard convolution, and the sampling points of their convolution kernels are fixed regions. However, TEC is dynamically changing, and predictions for the future may come from irregular regions. Therefore, it is very important to flexibly capture the changing characteristics in spatially irregular TEC regions.

SA-ConvLSTM [39] innovatively introduces self-attention memory into ConvLSTM, dynamically models the long-term spatial correlation of TEC through self-attention memory, and aggregates it with short-term memory. It solves the problem of ConvLSTM and ConvGRU obtaining long-term dependencies through convolution operations and effectively extracts long-term features, improving the modeling ability of the model for complex spatial dynamics of the ionosphere. Additionally, to extract irregular region features, we introduced deformable convolution [40] into SA-ConvLSTM and proposed a novel unit SA-DConvLSTM. This unit extracts features from irregular areas through learnable offsets. This is more effective for feature extraction of TEC. Building upon SA-DConvLSTM, we propose ED-SA-DConvLSTM, an encoder–decoder architecture for TEC spatiotemporal prediction. The encoder progressively transforms input TEC sequences into compressed spatiotemporal representations, while the decoder reconstructs these features into predicted TEC maps. The improvements in the paper allow for more flexible feature extraction of TEC while also better utilizing long-term spatial dependencies.

To evaluate model performance, we conducted experiments using a 6-year sequence of TEC maps (2013–2015, 2017–2019) covering the region of 12.5° S–87.5° N and 25° E–180° E.

This study region encompasses all of Asia and surrounding regions, allowing us to assess the model under both high and low solar activity periods.

The dataset was divided into 4 years of training and 2 years of testing. We compared ED-SA-DConvLSTM against three benchmarks: (1) ConvGRU and ConvLSTM as state-of-the-art spatiotemporal models, and (2) C1PG, which is a 1-day TEC prediction product provided by Center Orbit Determination Europe (CODE). In the above description, SA-ConvLSTM and ED-SA-DConvLSTM are already simplified forms of their original technical designations, where "SA" is "self-attention", "D" is "deformable convolution", and "ED" is "encoder–decoder architecture". The baseline models (C1PG, ConvLSTM, ConvGRU) are widely recognized in the field. C1PG is the official name of the IGS reference model. ConvLSTM and ConvGRU are canonical architectures.

2. Data and Data Processing

The experimental data consist of Global Ionospheric Maps (GIMs) provided by the International GNSS Service (IGS), stored in IONEX format files. Each IONEX file contains daily GIM data with a spatial resolution of 5° (longitude) × 2.5° (latitude) and a temporal resolution of 2 h, covering the global range from 87.5° S to 87.5° N and 180° W to 180° E.

Due to computational complexity, this study focuses on a specific subregion (25° E–180° E, 12.5° S–87.5° N) encompassing all of Asia and surrounding regions. The study region is illustrated in Figure 1. This area encompasses both equatorial and mid-latitude regions, including the Equatorial Ionization Anomaly (EIA) zone, making it both distinctive and representative. To account for the impact of solar activity on TEC predictions, the dataset includes TEC maps from three years of high solar activity (2013–2015) and three years of low solar activity (2017–2019). The data are partitioned into the training set (2013–2014, 2017–2018; 17,520 maps) and testing set (2015, 2019; 8760 maps).

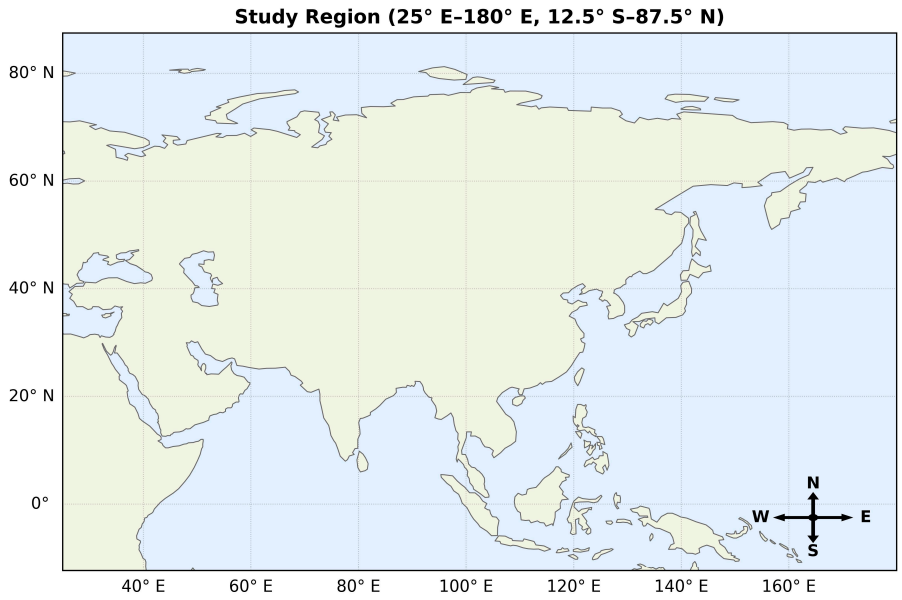


Figure 1. Map of the study area.

To mitigate data scale biases, we normalized all TEC values using Min-Max standardization, which transforms the data into a $[0, 1]$ range through linear scaling. The normalization formula is given by:

$$X' = \frac{X - X_{min}}{X_{max} - X_{min}} \quad (1)$$

where X is the original TEC map, X' denotes the normalized values constrained to the range $[0, 1]$, and X_{min} and X_{max} represent the minimum and maximum of X in the training set, respectively.

3. Methodology

In this paper, we first replaced the standard convolution of SA-ConvLSTM with deformable convolution and proposed SA-DConvLSTM. Then, a TEC spatiotemporal prediction model ED-SA-DConvLSTM is proposed based on SA-DConvLSTM as the basic blocks. This section provides a detailed introduction to the core technologies implemented.

3.1. The Original SA-ConvLSTM

SA-ConvLSTM extends the standard ConvLSTM by incorporating a self-attention memory (SAM) module. The following subsections detail the SAM and the SA-ConvLSTM.

3.1.1. Self-Attention Memory (SAM) Module

The SAM module takes two inputs: the current time step's feature H_t and the previous memory state M_{t-1}, which memorizes long-term spatial dependencies [39]. It outputs an updated memory state M_t and a fused feature $\hat{H}_t$. The detailed structure of SAM is shown in Figure 2.

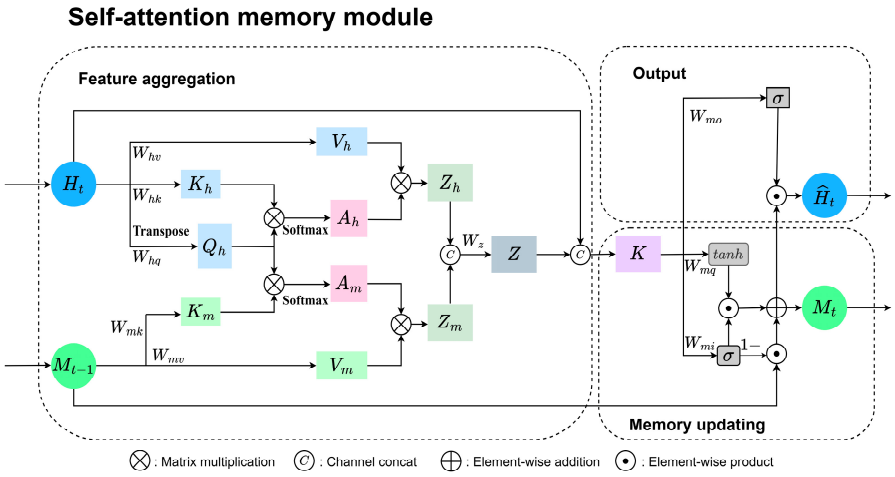


Figure 2. Basic structure of SAM module.

Specifically, the SAM module integrates three core operations: (1) feature aggregation, (2) memory updating, and (3) output.

- Feature aggregation:

This part first weights the current time step features and the long-term spatial memory features and then aggregates them together to form a new feature vector. The calculation process is as shown in Equations (2)–(4).

$$\begin{cases} K_h = W_{hk} H_t, Q_h = W_{hq} H_t, V_h = W_{hv} H_t \\ A_h = Q_h^T K_h \\ Z_h = A_h V_h \end{cases} \tag{2}$$

$$\begin{cases} K_m = W_{mk} M_{t-1}, Q_h = W_{hq} H_t, V_m = W_{mv} M_{t-1} \\ A_m = Q_h^T K_m \\ Z_m = A_m V_m \end{cases} \tag{3}$$

$$Z = W_Z [Z_h; Z_m] \tag{4}$$

In the above formulation, the weight A_h is first computed for the current feature H_t, generating the weighted feature Z_h. Similarly, the weight A_m is derived for the long-term memory state M_{t-1}, obtaining the weighted memory state Z_m. These two components, Z_h and Z_m, are then concatenated to form the aggregated feature vector Z. W_{hq}, W_{hk}, W_{hv}, W_{mk}, W_{mv}, W_z are weight matrices, and Q_h, K_h, K_m, V_h, V_m are the intermediate vectors that support the calculated attention scores.

- Memory updating:

This part is used for the adaptive updating of long-term spatial dependencies M_t, and the specific process is as follows:

$$\begin{cases} K = [H_t; Z] \\ i'_t = \sigma(W_{mi} * K + b_{mi}) \\ g'_t = tanh(W_{mg} * K + b_{mg}) \\ M_t = (1 - i'_t) \odot M_{t-1} + i'_t \odot g'_t \end{cases} \tag{5}$$

The gating mechanism computes the long-term memory features by combining the previous time step's memory with the current feature K, effectively capturing long-term dependencies.

- Output:

This part generates the output $\hat{H}_t$. The calculation process is as follows:

$$\begin{cases} o'_t = \sigma(W_{mo} * K + b_{mo}) \\ \hat{H}_t = o'_t \odot M_t \end{cases} \tag{6}$$

The pseudocode for the SAM calculation process is shown in Table 1.

Table 1. The pseudocode for the SAM calculation process.

Feature Aggregation	
1	Receive the short-term memory feature H_t of the current time step and the long-term memory feature M_{t-1} of the previous time step.
2	Obtain K_h, Q_h, V_h, K_m, V_m through linear transformations of H_t and M_{t-1}.
3	Calculate the similarity scores of H_t and M_{t-1} separately to obtain A_h, A_m.
4	Weight V_h and V_m separately to obtain Z_h and Z_m, and concatenate them to obtain Z.
5	Concatenate Z and H_t to obtain a new feature K.
Memory updating	
6	K and M_{t-1} are operated to obtain the long-term memory feature M_t of the current time step.
Output	
7	K and M_t are operated to obtain the updated short-term memory feature $\hat{H}_t$ of the current time step.

3.1.2. SA-ConvLSTM

The SA-ConvLSTM integrates the SAM module with ConvLSTM, as illustrated in Figure 2. Each unit contains three standard gates and the SAM module, with the complete computational process as follows:

$$\begin{cases} f_t = \sigma\left(W_{xf} * X_t + W_{hf} * \hat{H}_{t-1} + b_f\right) \\ i_t = \sigma\left(W_{xi} * X_t + W_{hi} * \hat{H}_{t-1} + b_i\right) \\ \hat{c}_t = \tanh\left(W_{xc} * X_t + W_{hc} * \hat{H}_{t-1} + b_c\right) \\ C_t = f_t \odot C_{t-1} + i_t \odot \hat{c}_t \\ o_t = \sigma\left(W_{xo} * X_t + W_{ho} * \hat{H}_{t-1} + b_o\right) \\ H_t = o_t \odot \tanh(C_t) \end{cases} \tag{7}$$

where X_t denotes the current input, H_t is the current feature extracted by ConvLSTM, and $\hat{H}_{t-1}$ represents the output from the previous time step.

3.2. SA-DConvLSTM

While the original SA-ConvLSTM employs standard convolution with fixed, regular receptive fields, this approach limits feature extraction to rigid patterns and struggles with complex deformations. To address this, deformable convolution [40] introduces learnable offsets to the sampling positions, enabling adaptive receptive field shapes. This modification allows the model to adaptively extract features from irregular regions, better adapting to TEC maps with continuous changes.

The calculation formulas for standard convolution and deformable convolution are Equations (8) and (9), respectively.

$$y(P_0) = \sum_{P_n \in R} w(P_n) \cdot x(P_0 + P_n) \tag{8}$$

$$y(P_0) = \sum_{P_n \in R} w(P_n) \cdot x(P_0 + P_n + \Delta P_n) \tag{9}$$

Among them, P_0 is an arbitrary position on the input feature map; P_n represents the offset of each point in the convolution kernel from the central point P_0; ΔP_n denotes the learnable offsets at position P_n; $x()$ is the value at a certain position on the input feature map; $w(P_n)$ is the weight at position P_n; $y(P_0)$ represents the result of convolution at position P_0; and R is a set that contains all the sampling points in the convolutional kernel.

Figure 3 illustrates the difference in sampling point distributions between standard convolution and deformable convolution. As shown in the figure, the sampling points of standard convolution (left) follow a fixed rectangular grid pattern with a rigid and non-learnable geometric structure. In contrast, deformable convolution (right) introduces learnable spatial offsets, allowing each sampling point to dynamically adjust its position based on target features. This flexible mechanism enables the convolutional kernel to adaptively conform to geometric deformations or complex structures of objects, significantly enhancing the model's ability to capture shape variations. The spatial arrangement of sampling points in the figure visually demonstrates the essential distinction between the two convolution methods in the feature extraction strategy.

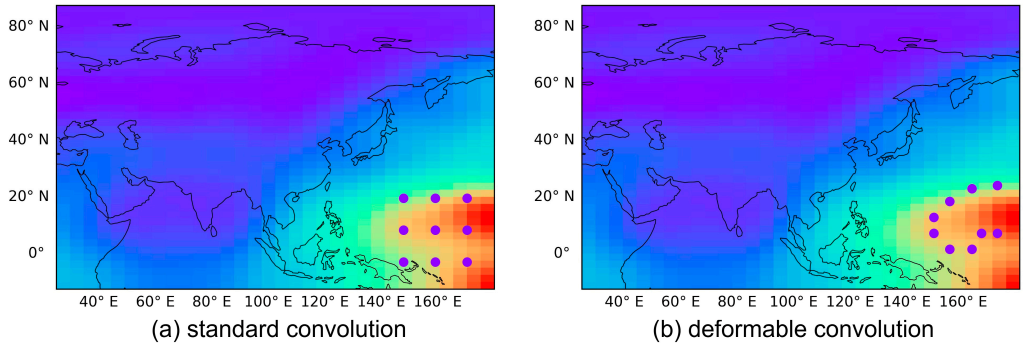


Figure 3. Comparison of sampling points of standard convolution and deformable convolution, in which purple dots are sampling points.

Considering the merit of deformable convolution, this paper embedded it into SA-ConvLSTM and proposed SA-DConvLSTM. The structure comparison between SA-ConvLSTM and SA-DConvLSTM is shown in Figure 4, where our improvements are marked in the blue box.

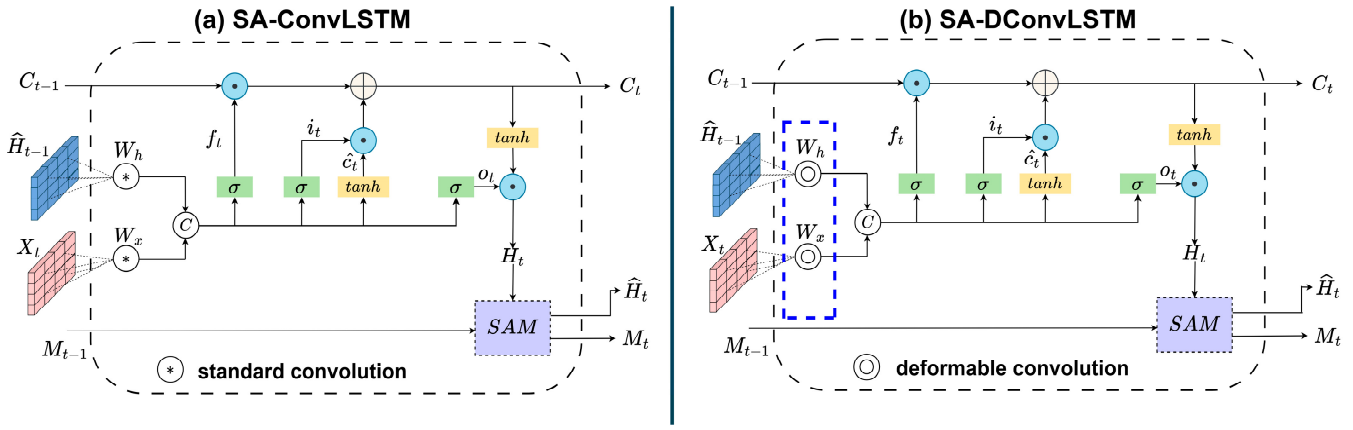


Figure 4. Structural comparison of SA-ConvLSTM and SA-DConvLSTM. Among them, the blue box is the improved part.

3.3. The Proposed ED-SA-DConvLSTM

On the basis of the SA-DConvLSTM units introduced earlier, we organized these units into an encoder–decoder architecture to construct our TEC spatiotemporal prediction model, called ED-SA-DConvLSTM. As shown in Figure 5, the model architecture consists of two parts: an encoder for feature extraction and a decoder for prediction generation.

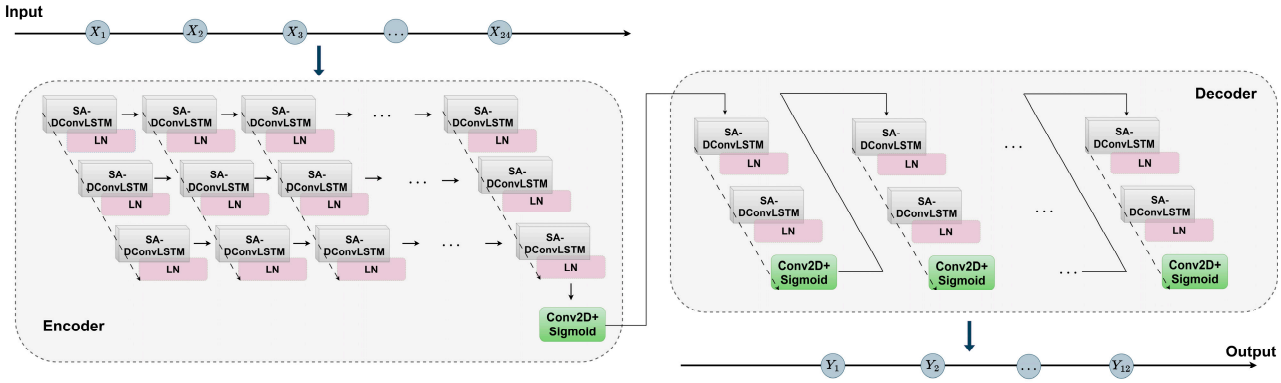


Figure 5. The structure of ED-SA-DConvLSTM.

The encoder processes input TEC map sequences through three consecutive SA-DConvLSTM layers, progressively extracting hierarchical spatiotemporal features. Each SA-DConvLSTM layer is followed by LayerNorm (LN) to stabilize activations and mitigate gradient issues. In the recurrent neural network, LN has more advantages [41]. The final Conv2D layer with sigmoid activation consolidates the feature sequences into a compressed representation. The decoder reconstructs the TEC predictions through two SA-DConvLSTM+LN layers, which progressively expand the encoded features into output sequences. Due to limited computing resources, this study manually selected the architecture design of a three-layer encoder and a two-layer decoder. Furthermore, based on the non-negative nature of TEC, we employed a sigmoid activation in the final layer to strictly constrain predictions within the normalized $[0, 1]$ range, ensuring the physical consistency of the results.

The ED-SA-DConvLSTM model processes an input TEC map sequence through its encoder to extract a compressed spatiotemporal feature representation, which the decoder then expands into a variable-length output sequence.

4. Experimental Results

4.1. Evaluation Metrics

This study employs two evaluation metrics to quantitatively assess model performance: Root Mean Square Error ($RMSE$) and Mean Absolute Percentage Error ($MAPE$). These metrics are calculated as follows:

$$RMSE = \sqrt{\frac{1}{n}\sum_{i=1}^{n}(y_i - \hat{y}_i)^2} \tag{10}$$

$$MAPE = \frac{1}{n}\sum_{i=1}^{n}\left|\frac{y_i - \hat{y}_i}{y_i}\right| \times 100\% \tag{11}$$

Among them, n is the number of samples in the test set, and y_i and $\hat{y}_i$ are the true and predicted values, respectively.

4.2. Model Optimization

In deep learning, hyperparameter configuration has a significant impact on model performance [42,43]. Hyperparameters are usually divided into two categories: model structure hyperparameters and training process hyperparameters. Automatically optimizing all hyperparameters requires a significant amount of time. Therefore, we manually optimized the architectural hyperparameters: using the adaptive motion estimation (ADAM) optimizer, mean square error (MSE) loss function, and CosineAnnealingWarmRestarts learning rate scheduling, with an initial value of 0.001, and adjusting it every 50 iterations; the maximum number of iterations is 200. The parameters (number and size of convolution kernels) in the training process are automatically tuned by the Bayesian optimization method. Among the benchmark models evaluated, C1PG serves as a non-trainable reference product provided by CODE. In contrast, the proposed ED-SA-DConvLSTM and comparison models (ConvGRU and ConvLSTM) require hyperparameter optimization. The final optimized values are shown in Table 2 and applied consistently in comparative experiments.

Table 2. The optimal hyperparameters obtained through Bayesian optimization.

Model	Hyperparameter Setting	
	The Number of Convolution Kernels	The Size of Convolution Kernels
ConvGRU	30	3
ConvLSTM	64	5
ED-SA-DConvLSTM	30	3

4.3. The Input and Output Length

This subsection identifies the optimal time window configuration for the model. As shown in Figure 6, a 2-day input window demonstrates superior prediction accuracy across varying solar activity levels, with $RMSEs$ of 3.5777 $TECU$ and 1.3417 $TECU$ in high and low solar activity, respectively. Consequently, all subsequent experiments employ this optimal "2-day input to 1-day output" configuration.

4.4. Ablation Experiment

This subsection validates the effectiveness of deformable convolution through an ablation experiment. Table 3 shows the results of the ablation experiment, where the only difference between ED-SA-ConvLSTM and ED-SA-DConvLSTM is the use of standard convolution in ED-SA-ConvLSTM and deformable convolution in ED-SA-DConvLSTM. It can be seen that after adding deformable convolution, the $RMSEs$ decreased by 1.03% in 2015 and 0.94% in 2019. This indicates that deformable convolution can improve the performance of the model.

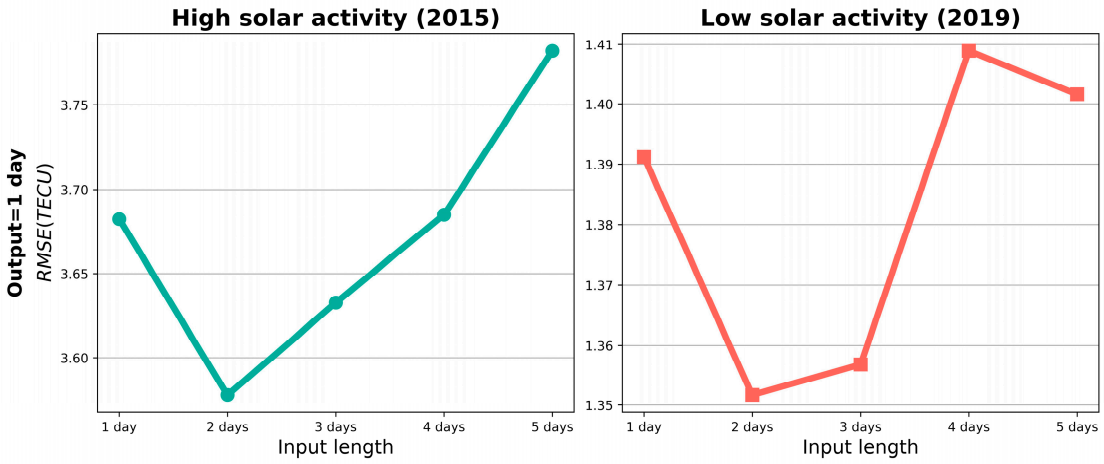


Figure 6. The impact of different input lengths on prediction performance.

Table 3. Comparison results of ablation experiment.

Solar Activity	Model	*RMSE*(*TECU*)	Improved
High solar activity (2015)	ED-SA-ConvLSTM	3.6150	--
	ED-SA-DConvLSTM	3.5777	1.03%
Low solar activity (2019)	ED-SA-ConvLSTM	1.3645	--
	ED-SA-DConvLSTM	1.3517	0.94%

4.5. Comparison with Other Models

4.5.1. Overall Quantitative Comparison

As evidenced in Table 4, the proposed ED-SA-DConvLSTM demonstrates superior predictive performance compared to all benchmark models (C1PG, ConvGRU, and ConvLSTM) across both solar activities. During high solar activity (2015), the model achieves *RMSE* reductions of 10.27%, 7.65%, and 7.16% relative to C1PG, ConvGRU, and ConvLSTM, respectively, while under low solar activity (2019), these improvements reach 11.46%, 4.75%, and 4.06%. Furthermore, ED-SA-DConvLSTM consistently delivers the lowest MAPE in both solar activities.

Table 4. Overall comparison on the test set (the best are bolded).

Solar Activity	Model	*RMSE*(*TECU*)	*MAPE*
2015 (High)	C1PG	4.0295	16.12%
	ConvGRU	3.9144	14.76%
	ConvLSTM	3.8936	14.47%
	ED-SA-DConvLSTM	**3.5777**	**13.20%**
2019 (Low)	C1PG	1.5421	14.95%
	ConvGRU	1.4325	14.70%
	ConvLSTM	1.4222	14.01%
	ED-SA-DConvLSTM	**1.3517**	**13.72%**

Figure 7 further illustrates the pairwise comparison of error distributions between ED-SA-DConvLSTM and three other comparative models. In Figure 5, the left side represents high solar activity, and the right side represents low solar activity. The horizontal axis of each subgraph represents the prediction error value Δ ($\Delta = predicted\ value - true\ value$) of the model, and the vertical axis represents the proportion of Δ in each interval. ED-SA-DConvLSTM shows higher proportions of zero-error predictions ($\Delta = 0$) than C1PG, ConvGRU, and ConvLSTM, demonstrating its superior TEC prediction accuracy.

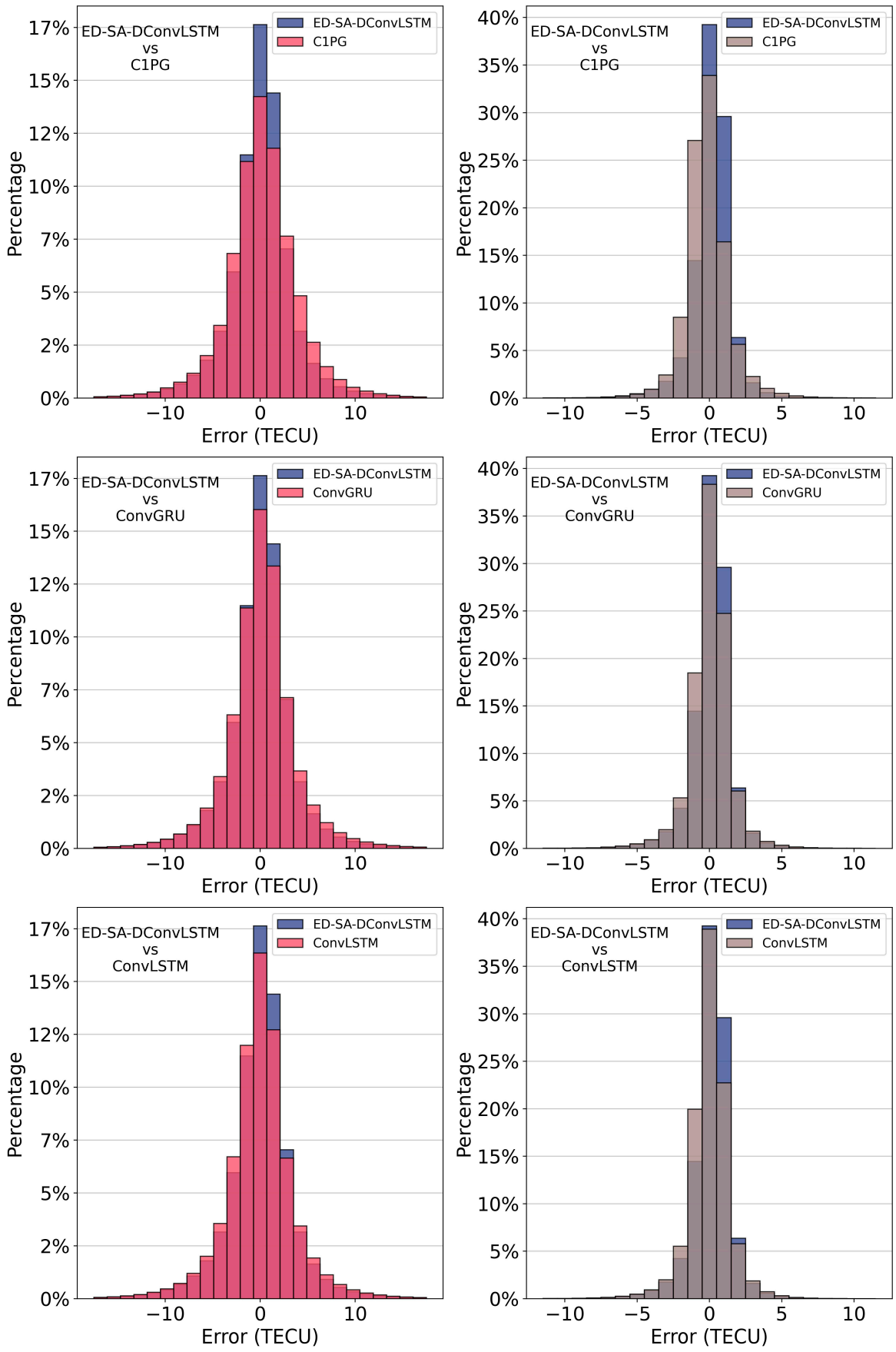


Figure 7. Error pairwise comparison histogram.

4.5.2. Visual Comparison of Various Models

To visually compare the prediction performance of different models, we selected one day during high solar activity (DOY 196, 2015) and low solar activity (DOY 196, 2019), presenting TEC prediction maps and corresponding absolute error maps at two representative time points (UT 0:00 and UT 12:00), as shown in Figures 8 and 9, respectively. The *RMSE* is marked in Figure 7 (with the minimum value in red). The results indicate that the proposed ED-SA-DConvLSTM achieves the lowest *RMSE* among all models, particularly in the Equatorial Ionization Anomaly (EIA) region, demonstrating its superior ability to capture TEC variations.

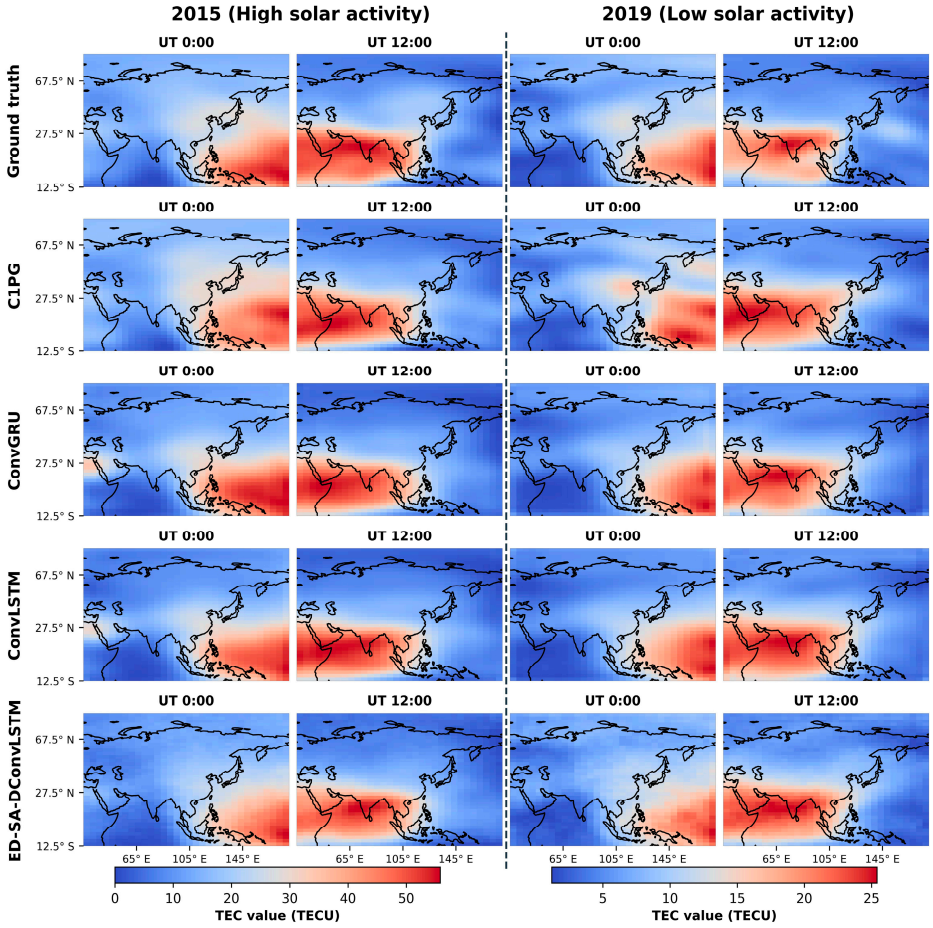


Figure 8. Visual effects of various models.

4.5.3. Comparison Under Extreme Situations

To evaluate model robustness under extreme situations, we specifically selected four geomagnetic storm events in 2015, as shown in Figure 10. Geomagnetic storm can cause severe ionospheric disturbances, seriously challenging the accuracy of TEC prediction [44]. Each event is analyzed using continuous 3-day TEC maps centered on the minimum Dst index, capturing the complete disturbance cycle from initial onset through the recovery phase.

We first calculated the *RMSE* of all models for each geomagnetic storm event and the improvement of ED-SA-DConvLSTM compared to C1PG, ConvGRU, and ConvLSTM, as shown in Table 5. The results demonstrated that the ED-SA-DConvLSTM consistently achieved the lowest *RMSE* across all four geomagnetic storm events, exhibiting superior prediction performance throughout the entire storm period. These proved that the ED-SA-DConvLSTM has more stable prediction ability during the whole geomagnetic storm.

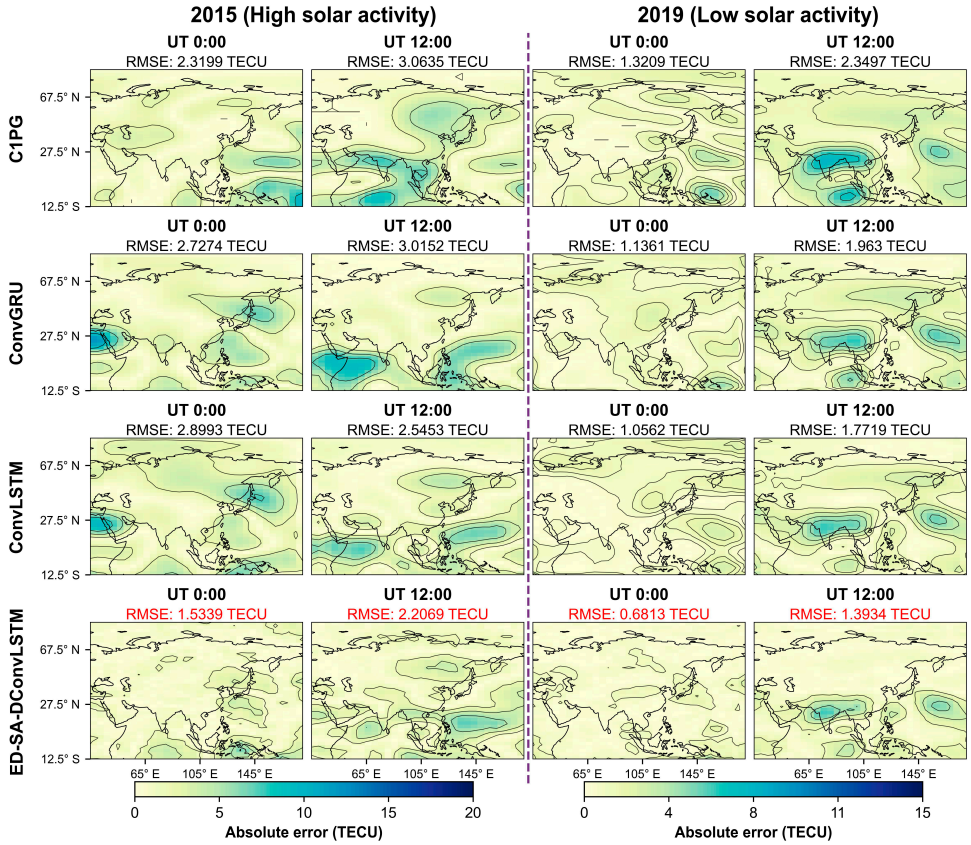


Figure 9. Absolute error map of each model.

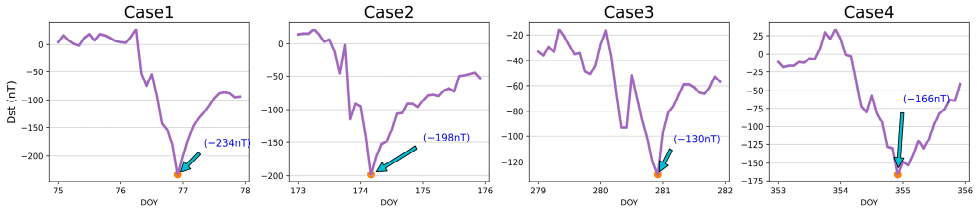


Figure 10. The selection of geomagnetic storm events in 2015. The orange point pointed by the green arrow is the minimum Dst index.

Table 5. *RMSE* of all models during geomagnetic storm events and relative improvements by ED-SA-DConvLSTM.

Events	Model	*RMSE*(*TECU*)	Improvement (C1PG/ConvGRU/ConvLSTM)
Case 1	C1PG	8.9381	-
	ConvGRU	9.2155	-
	ConvLSTM	9.0865	-
	ED-SA-DConvLSTM	6.3869	+28.5%/+30.7%/+29.7%
Case 2	C1PG	5.0921	-
	ConvGRU	5.5086	-
	ConvLSTM	5.2444	-
	ED-SA-DConvLSTM	4.0530	+20.4%/+26.4%/+22.7%
Case 3	C1PG	4.0527	-
	ConvGRU	4.2831	-
	ConvLSTM	4.2376	-
	ED-SA-DConvLSTM	3.6020	+11.1%/+15.9%/+15.0%
Case 4	C1PG	5.7812	-
	ConvGRU	5.6792	-
	ConvLSTM	5.8194	-
	ED-SA-DConvLSTM	4.8164	+16.6%/+15.1%/+17.2%

To further evaluate the performance of the model, we conducted a fine-grained comparison by calculating the *RMSE* of each model at each time step and visualized the results in Figure 11. The top-left corner of the figure indicates the percentage of time steps where ED-SA-DConvLSTM outperforms the other three baseline models.

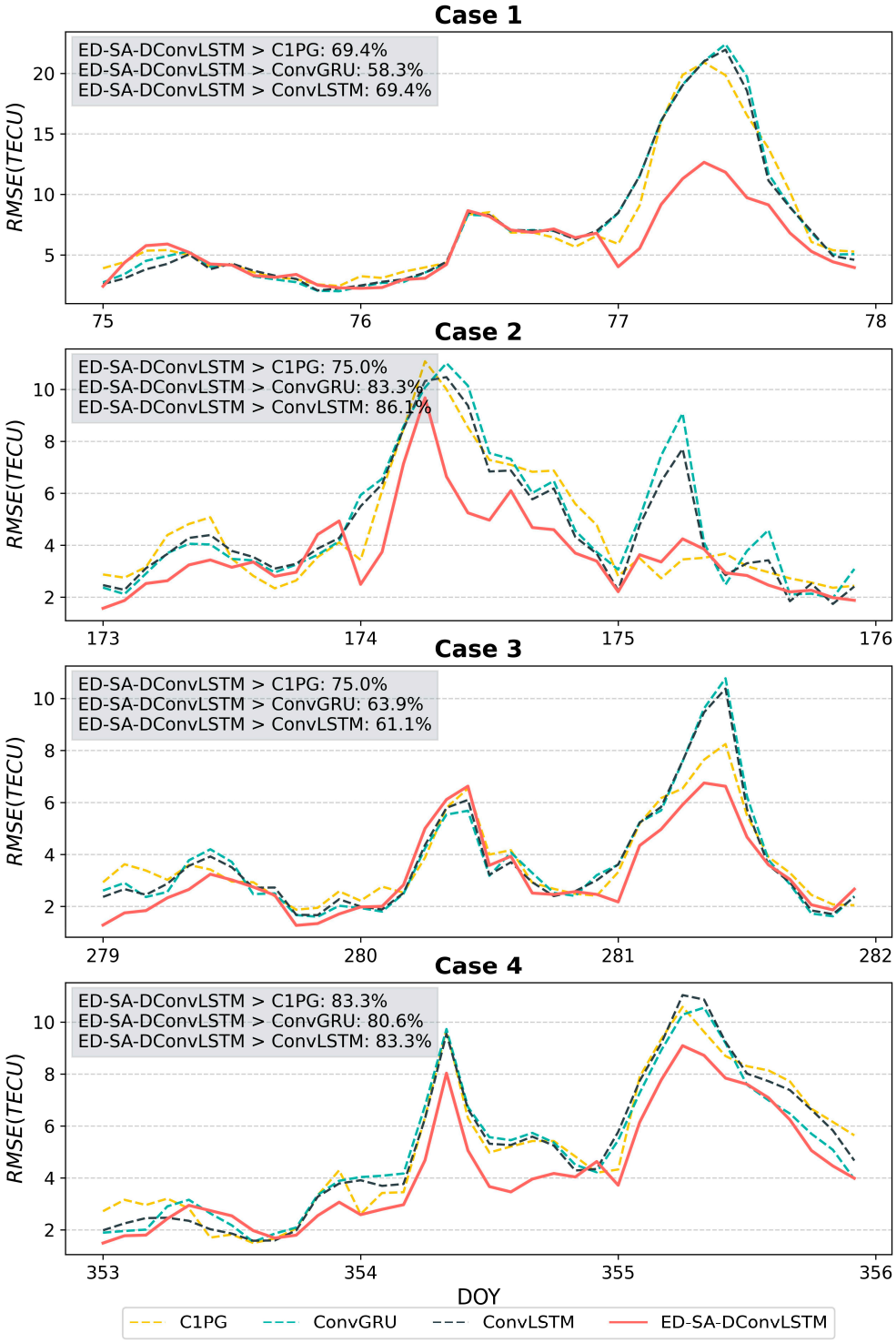


Figure 11. *RMSE* comparison of each model in different geomagnetic storm events.

Statistical results demonstrated that ED-SA-DConvLSTM achieves a lower *RMSE* than baseline models (C1PG, ConvGRU, and ConvLSTM) in 58.3–86.3% of all time points across all cases, with all proportions exceeding 50%. While the ED-SA-DConvLSTM exhibits

substantial superiority in aggregate predictive performance, its forecasting efficacy still has room for improvement owing to the complex nature of geomagnetic storms. This constraint underscores the persistent challenges in extreme situation event prediction.

5. Conclusions

This paper proposed ED-SA-DConvLSTM, an encoder–decoder architecture for TEC spatiotemporal prediction, with the SA-DConvLSTM unit as the basic block. This proposed model uses the SAM module to capture long-term spatial dependencies and integrates them with short-term spatial dependencies. Furthermore, by replacing standard convolution with deformable convolution, the model overcomes the rigid receptive field limitations of SA-ConvLSTM, enabling adaptive feature extraction from irregular regions. This facilitates the modeling of dynamic, long-term spatial dependencies and the adaptive extraction of complex features in TEC.

To evaluate the performance, the proposed ED-SA-DConvLSTM was compared with two state-of-the-art deep learning models (ConvGRU and ConvLSTM) and a TEC prediction product C1PG, including overall quantitative comparison and comparison under extreme situations. The overall quantitative comparison experiment shows that the $RMSE$ of our model is reduced by 10.27%, 7.65%, and 7.16% compared with those of C1PG, ConvGRU, and ConvLSTM, respectively, in high solar activity. In low solar activity, it decreased by 11.46%, 4.75%, and 4.06%, respectively. In the four geomagnetic storm events, the $RMSE$ of ED-SA-DConvLSTM outperformed the comparison models in most cases. Their proportions all exceeded 58%.

Currently, our research primarily focuses on improving prediction accuracy. In future work, we will conduct user evaluations and operational adaptation and further investigate the underlying physical mechanisms. Meanwhile, when sufficient computational resources become available, we will extend the prediction capability to global scales.

Author Contributions: Methodology, J.L. and J.X.; software, J.L. and J.X.; validation, X.D. and S.L.; investigation, X.D. and S.L.; resources, J.L.; writing—original draft preparation, J.L. and J.X.; writing—review and editing, H.L. All authors have read and agreed to the published version of the manuscript.

Funding: This research received no external funding.

Institutional Review Board Statement: Not applicable.

Informed Consent Statement: Not applicable.

Data Availability Statement: The International GNSS Service (IGS) final product and the CODE 1-day prediction product (C1PG) were both downloaded from NASA's CDDIS archive [45] (https://cddis.nasa.gov/archive/gnss/products/ionex/) (accessed on 7 July 2025).

Acknowledgments: We gratefully acknowledge the IGS and CODE teams for their ongoing efforts in sustaining and enhancing these essential resources for researchers worldwide.

Conflicts of Interest: The authors declare no conflicts of interest. Author Jie Li, Xiaofeng Du and Shixiang Liu was employed by the company "China National Offshore Oil Corporation Research Institute, Co., Ltd.". The remaining authors declare that the research was conducted in the absence of any commercial or financial relationships that could be construed as a potential conflict of interest.

References

1. Wang, H.; Liu, H.; Yuan, J.; Le, H.; Shan, W.; Li, L. MAOOA-Residual-Attention-BiConvLSTM: An Automated Deep Learning Framework for Global TEC Map Prediction. *Space Weather* **2024**, *22*, e2024SW003954. [CrossRef]
2. Komjathy, A.; Langley, R.B. An Assessment of Predicted and Measured Ionospheric Total Electron Content Using a Regional GPS Network. In Proceedings of the 1996 National Technical Meeting of The Institute of Navigation, Santa Monica, CA, USA, 22–24 January 1996.
3. Gao, X.; Yao, Y. A Storm-Time Ionospheric TEC Model with Multichannel Features by the Spatiotemporal ConvLSTM Network. *J. Geod.* **2023**, *97*, 9. [CrossRef]
4. Nishioka, M.; Saito, S.; Tao, C.; Shiota, D.; Tsugawa, T.; Ishii, M. Statistical Analysis of Ionospheric Total Electron Content (TEC): Long-Term Estimation of Extreme TEC in Japan. *Earth Planets Space* **2021**, *73*, 52. [CrossRef]
5. Mannucci, A.J.; Wilson, B.D.; Yuan, D.N.; Ho, C.H.; Lindqwister, U.J.; Runge, T.F. A Global Mapping Technique for GPS-Derived Ionospheric Total Electron Content Measurements. *Radio Sci.* **1998**, *33*, 565–582. [CrossRef]
6. Jakowski, N.; Mayer, C.; Hoque, M.M.; Wilken, V. Total Electron Content Models and Their Use in Ionosphere Monitoring. *Radio Sci.* **2011**, *46*, 1–11. [CrossRef]
7. Sardón, E.; Rius, A.; Zarraoa, N. Estimation of the Transmitter and Receiver Differential Biases and the Ionospheric Total Electron Content from Global Positioning System Observations. *Radio Sci.* **1994**, *29*, 577–586. [CrossRef]
8. Zhukov, A.V.; Yasyukevich, Y.V.; Bykov, A.E. Correction to: GIMLi: Global Ionospheric Total Electron Content Model Based on Machine Learning. *GPS Solut.* **2020**, *25*, 21. [CrossRef]
9. Lean, J.L.; Emmert, J.T.; Picone, J.M.; Meier, R.R. Global and Regional Trends in Ionospheric Total Electron Content. *J. Geophys. Res. Space Phys.* **2011**, *116*. [CrossRef]
10. Sivavaraprasad, G.; Deepika, V.S.; SreenivasaRao, D.; Ravi Kumar, M.; Sridhar, M. Performance Evaluation of Neural Network TEC Forecasting Models over Equatorial Low-Latitude Indian GNSS Station. *Geod. Geodyn.* **2020**, *11*, 192–201. [CrossRef]
11. Saharan, S.; Maurya, A.K.; Dube, A.; Patil, O.M.; Singh, R.; Sharma, H. Low Latitude Ionospheric TEC Response to the Solar Flares during the Peak of Solar Cycle 24. *Adv. Space Res.* **2023**, *72*, 3890–3902. [CrossRef]
12. Hu, T.; Lei, Y.; Su, J.; Yang, H.; Ni, W.; Gao, C.; Yu, J.; Wang, Y.; Gu, Y. Learning Spatiotemporal Features of DSA Using 3D CNN and BiConvGRU for Ischemic Moyamoya Disease Detection. *Int. J. Neurosci.* **2023**, *133*, 512–522. [CrossRef]
13. Wang, D.; Yang, Y.; Ning, S. DeepSTCL: A Deep Spatio-Temporal ConvLSTM for Travel Demand Prediction. In Proceedings of the 2018 International Joint Conference on Neural Networks (IJCNN), Rio de Janeiro, Brazil, 8–13 July 2018; pp. 1–8.
14. Wang, X.; Xie, W.; Song, J. Learning Spatiotemporal Features with 3DCNN and ConvGRU for Video Anomaly Detection. In Proceedings of the 2018 14th IEEE International Conference on Signal Processing (ICSP), Beijing, China, 12–16 August 2018; pp. 474–479.
15. Jiang, Z.; Zhang, Z.; He, X.; Li, Y.; Yuan, H. Efficient and Accurate TEC Modeling and Prediction Approach with Random Forest and Bi-LSTM for Large-Scale Region. *Adv. Space Res.* **2024**, *73*, 650–662. [CrossRef]
16. Liu, L.; Zou, S.; Yao, Y.; Wang, Z. Forecasting Global Ionospheric TEC Using Deep Learning Approach. *Space Weather* **2020**, *18*, e2020SW002501. [CrossRef]
17. Wen, Z.; Li, S.; Li, L.; Wu, B.; Fu, J. Ionospheric TEC Prediction Using Long Short-Term Memory Deep Learning Network. *Astrophys. Space Sci.* **2021**, *366*, 3. [CrossRef]
18. Alemu, G.B.; Ejigu, Y.G. Prediction of Ionospheric Total Electron Content over Low Latitude Region: Case Study in Ethiopia. *Adv. Space Res.* **2024**, *74*, 284–302. [CrossRef]
19. Sun, W.; Xu, L.; Huang, X.; Zhang, W.; Yuan, T.; Chen, Z.; Yan, Y. Forecasting of Ionospheric Vertical Total Electron Content (TEC) Using LSTM Networks. In Proceedings of the 2017 International Conference on Machine Learning and Cybernetics (ICMLC), Nanjing, China, 9–11 July 2017; Volume 2, pp. 340–344.
20. Xie, T.; Dai, Z.; Zhu, X.; Chen, B.; Ran, C. LSTM-Based Short-Term Ionospheric TEC Forecast Model and Positioning Accuracy Analysis. *GPS Solut.* **2023**, *27*, 66. [CrossRef]
21. Tang, J.; Liu, C.; Yang, D.; Ding, M. Prediction of Ionospheric TEC Using a GRU Mechanism Method. *Adv. Space Res.* **2024**, *74*, 260–270. [CrossRef]
22. Li, D.; Jin, Y.; Wu, F.; Zhao, J.; Min, P.; Luo, X. A Hybrid Model for TEC Prediction Using BiLSTM and PSO-LSSVM. *Adv. Space Res.* **2024**, *74*, 303–318. [CrossRef]
23. Maheswaran, V.K.; Baskaradas, J.A.; Nagarajan, R.; Anbazhagan, R.; Subramanian, S.; Devanaboyina, V.R.; Das, R.M. Bi-LSTM Based Vertical Total Electron Content Prediction at Low-Latitude Equatorial Ionization Anomaly Region of South India. *Adv. Space Res.* **2024**, *73*, 3782–3796. [CrossRef]
24. Mao, S.; Li, H.; Zhang, Y.; Shi, Y. Prediction of Ionospheric Electron Density Distribution Based on CNN-LSTM Model. *IEEE Geosci. Remote Sens. Lett.* **2024**, *21*, 1–5. [CrossRef]

25. Kaselimi, M.; Doulamis, N.; Voulodimos, A.; Doulamis, A.; Delikaraoglou, D. Spatio-Temporal Ionospheric TEC Prediction Using a Deep CNN-GRU Model on GNSS Measurements. In Proceedings of the 2021 IEEE International Geoscience and Remote Sensing Symposium IGARSS, Brussels, Belgium, 11 July 2021; pp. 8317–8320.
26. Ren, X.; Zhao, B.; Ren, Z.; Wang, Y.; Xiong, B. Deep Learning-Based Prediction of Global Ionospheric TEC During Storm Periods: Mixed CNN-BiLSTM Method. *Space Weather* **2024**, *22*, e2024SW003877. [CrossRef]
27. Han, C.; Guo, Y.; Ou, M.; Wang, D.; Song, C.; Jin, R.; Zhen, W.; Bai, P.; Chong, X.; Wang, X. A Lightweight Prediction Model for Global Ionospheric Total Electron Content Based on Attention-BiLSTM. *Adv. Space Res.* **2024**, *75*, 3614–3629. [CrossRef]
28. Liu, H.; Wang, H.; Yuan, J.; Li, L.; Zhang, L. TEC Prediction Based on Att-CNN-BiLSTM. *IEEE Access* **2024**, *12*, 68471–68484. [CrossRef]
29. Shi, X.; Chen, Z.; Wang, H.; Yeung, D.-Y.; Wong, W.; Woo, W. Convolutional LSTM Network: A Machine Learning Approach for Precipitation Nowcasting. In Proceedings of the Advances in Neural Information Processing Systems, Montreal, QC, Canada, 7–12 December 2015; Volume 28.
30. Chen, J.; Zhi, N.; Liao, H.; Lu, M.; Feng, S. Global Forecasting of Ionospheric Vertical Total Electron Contents via ConvLSTM with Spectrum Analysis. *GPS Solut.* **2022**, *26*, 69. [CrossRef]
31. Liu, L.; Morton, Y.J.; Liu, Y. ML Prediction of Global Ionospheric TEC Maps. *Space Weather* **2022**, *20*, e2022SW003135. [CrossRef]
32. Xu, C.; Ding, M.; Tang, J. Prediction of GNSS-Based Regional Ionospheric TEC Using a Multichannel ConvLSTM with Attention Mechanism. *IEEE Geosci. Remote Sens. Lett.* **2024**, *21*, 1–5. [CrossRef]
33. Li, L.; Liu, H.; Le, H.; Yuan, J.; Shan, W.; Han, Y.; Yuan, G.; Cui, C.; Wang, J. Spatiotemporal Prediction of Ionospheric Total Electron Content Based on ED-ConvLSTM. *Remote Sens.* **2023**, *15*, 3064. [CrossRef]
34. de Paulo, M.C.M.; Marques, H.A.; Feitosa, R.Q.; Ferreira, M.P. New Encoder–Decoder Convolutional LSTM Neural Network Architectures for next-Day Global Ionosphere Maps Forecast. *GPS Solut.* **2023**, *27*, 95. [CrossRef]
35. Yang, J.; Huang, W.; Xia, G.; Zhou, C.; Chen, Y. Operational Forecasting of Global Ionospheric TEC Maps 1-, 2-, and 3-Day in Advance by ConvLSTM Model. *Remote Sens.* **2024**, *16*, 1700. [CrossRef]
36. Tang, J.; Zhong, Z.; Ding, M.; Yang, D.; Liu, H. Forecast of Ionospheric TEC Maps Using ConvGRU Deep Learning Over China. *IEEE J. Sel. Top. Appl. Earth Obs. Remote Sens.* **2024**, *17*, 3334–3344. [CrossRef]
37. Tang, J.; Zhong, Z.; Hu, J.; Wu, X. Forecasting Regional Ionospheric TEC Maps over China Using BiConvGRU Deep Learning. *Remote Sens.* **2023**, *15*, 3405. [CrossRef]
38. Luo, W.; Li, Y.; Urtasun, R.; Zemel, R. Understanding the Effective Receptive Field in Deep Convolutional Neural Networks. In *Advances in Neural Information Processing Systems*; The MIT Press: Cambridge, MA, USA, 2016; Volume 29.
39. Lin, Z.; Li, M.; Zheng, Z.; Cheng, Y.; Yuan, C. Self-Attention ConvLSTM for Spatiotemporal Prediction. *Proc. AAAI Conf. Artif. Intell.* **2022**, *34*, 11531–11538. [CrossRef]
40. Dai, J.; Qi, H.; Xiong, Y.; Li, Y.; Zhang, G.; Hu, H.; Wei, Y. Deformable Convolutional Networks. In Proceedings of the 2017 IEEE International Conference on Computer Vision (ICCV), Venice, Italy, 22–29 October 2017; pp. 764–773.
41. Ba, J.L.; Kiros, J.R.; Hinton, G.E. Layer Normalization. *arXiv* **2016**, arXiv:1607.06450.
42. Lavesson, N.; Davidsson, P. Quantifying the Impact of Learning Algorithm Parameter Tuning. *Proc. AAAI Conf. Artif. Intell.* **2006**, *6*, 395–400.
43. Weerts, H.J.P.; Mueller, A.C.; Vanschoren, J. Importance of Tuning Hyperparameters of Machine Learning Algorithms. *arXiv* **2020**, arXiv:2007.07588.
44. Blagoveshchensky, D.V.; Maltseva, O.A.; Sergeeva, M.A. Impact of Magnetic Storms on the Global TEC Distribution. *Ann. Geophys.* **2018**, *36*, 1057–1071. [CrossRef]
45. Noll, C.E. The Crustal Dynamics Data Information System: A Resource to Support Scientific Analysis Using Space Geodesy. *Adv. Space Res.* **2010**, *45*, 1421–1440. [CrossRef]

Disclaimer/Publisher's Note: The statements, opinions and data contained in all publications are solely those of the individual author(s) and contributor(s) and not of MDPI and/or the editor(s). MDPI and/or the editor(s) disclaim responsibility for any injury to people or property resulting from any ideas, methods, instructions or products referred to in the content.